ISSN 0021-3640, JETP Letters, 2010, Vol. 91, No. 9, pp. 471–477. © Pleiades Publishing, Inc., 2010.
Original Russian Text © M.B. Agranat, S.I. Anisimov, S.I. Ashitkov, V.V. Zhakhovskii, N.A. Inogamov, P.S. Komarov, A.V. Ovchinnikov, V.E. Fortov, V.A. Khokhlov, V.V. Shepelev, 2010, published in Pis'ma v Zhurnal Éksperimental'noĭ i Teoreticheskoĭ Fiziki, 2010, Vol. 91, No. 9, pp. 517–523.

Strength Properties of an Aluminum Melt at Extremely High Tension Rates under the Action of Femtosecond Laser Pulses

M. B. Agranat[a], S. I. Anisimov[b], S. I. Ashitkov[a], V. V. Zhakhovskii[a],
N. A. Inogamov[b], P. S. Komarov[a], A. V. Ovchinnikov[a],
V. E. Fortov[a], V. A. Khokhlov[b], and V. V. Shepelev[c]
[a] *Joint Institute for High Temperatures, Russian Academy of Sciences,*
ul. Izhorskaya 13/19, Moscow, 125412 Russia
[b] *Landau Institute for Theoretical Physics, Russian Academy of Sciences,*
Chernogolovka, Moscow region, 142432 Russia
e-mail: nailinogamov@googlemail.com
[c] *Institute for Computer Aided Design, Russian Academy of Sciences,*
Vtoraya Brestskaya ul. 19/18, Moscow, 123056 Russia

Received March 26, 2010

The dynamics of the melting of a surface nanolayer and the formation of thermal and shock waves in metals irradiated by femtosecond laser pulses has been investigated both experimentally and theoretically. A new experimental–computational method has been implemented to determine the parameters of laser-induced shock waves in metallic films. Data on the strength properties of the condensed phase in aluminum films at an extremely high strain rate ($\dot{V}/V \sim 10^9$ s^{-1})under the action of a laser-induced shock wave have been obtained.

DOI: 10.1134/S0021364010090080

The physical processes in condensed matter irradiated by femtosecond laser pulses with moderate intensities of 10^{11}–10^{13} W/cm^2 have been actively investigated in recent years. In addition to the technological aspects of the precision treatment of materials, investigations of the thermodynamic and strength characteristics of the surface nanolayer of a substance under the action of extremely short pump pulses are of great interest. Femtosecond interference microscopy [1–3] is one of the informative optical methods that make it possible to follow with a high accuracy the high-rate deformation of the substance caused by the action of femtosecond laser pulses. The corresponding space and time ranges of the measurements are 1–1000 nm and 0.1–1000 ps, respectively. In this respect, the measurements with the application of femtosecond interference microscopy miniaturize larger scale and slower methods of the Doppler velocity interferometer system for any reflector (VISAR) and the optically recording velocity interferometer system (ORVIS), which have exclusive significance for the diagnostics of pulse phenomena in the microsecond and nanosecond ranges [4–6]. The VISAR or ORVIS is used to analyze the dynamics of acoustic perturbations inside plates with thicknesses from tens of microns to millimeters.

Very high strain rates of materials $\dot{V}/V \sim 10^9$–10^{10} s^{-1} are associated with femtosecond laser pulses and submicron films. The diagnostics of the processes initiated by femtosecond laser pulses in metals is of great interest. For this reason, the experiments described below and the numerical simulation of the action of femtosecond laser pulses on thin aluminum films were performed. The time dependence of the displacement $\Delta x(t)$ of the rear surface (opposite to the heated surface) of a thin film was measured using femtosecond interference microscopy. This displacement is caused by the action of an acoustic wave excited owing to the heating of the front surface by femtosecond laser pulses. Then, the events occurring inside the irradiated film were reconstructed by means of the two-temperature hydrodynamic and molecular dynamics simulation from the function $\Delta x(t)$.

In this work, a titanium–sapphire laser system generating pulses with an energy of up to 2 mJ and a duration of $\tau_{\mathrm{FWHM}} = 40$ fs at a wavelength of 800 nm was used as a source of femtosecond laser pulses. Aluminum films with various thicknesses deposited by the magnetron sputtering method on 150-μm thin glass substrates were used as targets. A pump pulse (whose wavelength is $\lambda_{\mathrm{pump}} = 800$ nm) generating an acoustic wave in the sample was focused on the metal–glass interface through a 150-μm thin glass substrate in the normal direction to the target surface by a lens with a focal length of 150 mm (see Fig. 1). The $\Delta x(t)$ dependence was measured by femtosecond interference microscopy using a Michelson interferometer [2].

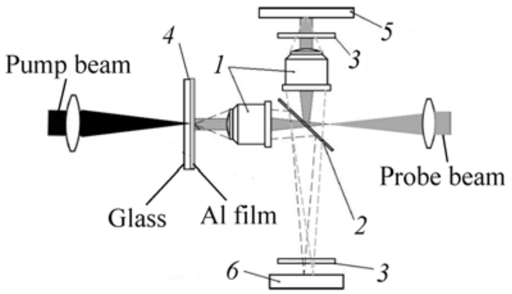

Fig. 1. Layout of the experiment: (*1*) microobjective, (*2*) beam splitter, (*3*) light filter, (*4*) target, (*5*) reference mirror, and (*6*) CCD matrix.

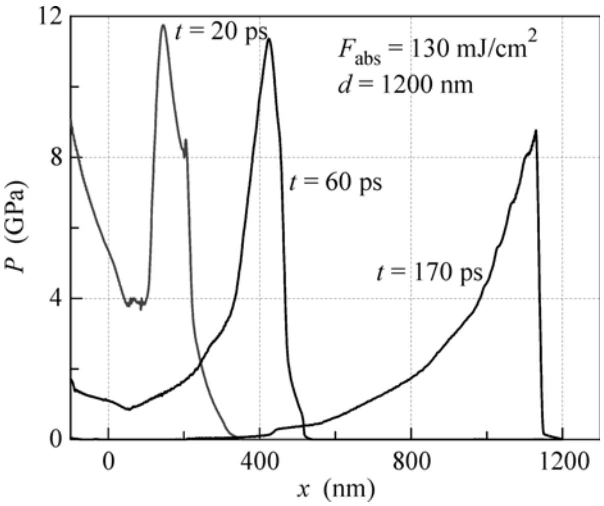

Fig. 2. Propagation of the compression wave p_+ from the heated layer d_T near the interface $x \approx 0$ towards the rear surface $x = d$. The shock wave in glass (at $x < 0$) is not shown, because the evolution of the wave p_+ in the film and the action of this wave on the rear surface are of interest.

Probing was performed by pulses of the second harmonic of the laser whose wavelength was λ_{probe} = 400 nm. The time interval between the pump and probe pulses was measured using an optical delay line. The high accuracy of the measurement of the phase of the reflected probe wave (a phase error of about $\approx\pi/200$) was reached by the application of the algorithm of the two-dimensional Fourier analysis of interference patterns and the procedure of the normalization of images [1, 2, 7]. The optical scheme and the methods of the measurements and analysis of interference patterns were described in [1–3]. A target was displaced to a new place by means of a three-coordinate microhandler after each pump pulse. The accuracy of the positioning of the rear surface of the target with respect to the object plane of the microobjective of the interferometer was no more than 1–2 μm and was controlled in terms of the contrast of the interference fringes.

To create the necessary pressure in the acoustic wave and prevent the development of nonlinear self-focusing and absorption processes in glass [8], which distort the spatial distribution of radiation at the focus and prevent an increase in the pressure with the energy of the pump pulse, the duration of the pulses was increased to $\tau_{\text{FWHM}} = 150$ fs. The time resolution of the measurements at this duration was about 200 fs. The spatial distribution of pump radiation at the focus in the experiments was Gaussian with a diameter of 80 μm at a level of $1/e$, which was much larger than the thicknesses $d = 350$ and 1200 nm of the used metallic films. This ensured the applicability of the one-dimensional approximation to the numerical simulation of the processes under investigation.

Let us present the picture of the absorption of laser radiation, the heating of the metal, and the generation of the acoustic signal. The absorption of femtosecond laser pulses strongly overheats the electron subsystem [3, 9]. Correspondingly, degeneracy is partially lifted during the action of a femtosecond laser pulse; for this reason, the electron–electron relaxation time is small, $t_{ee} \sim 10$ fs. Therefore, the two-temperature situation appears in the time interval $t_{ee} < t < t_{\text{eq}}$. The relaxation time to the one-temperature state at the used fluences was $t_{\text{eq}} \sim 3$–4 ps. The heated layer is primarily formed at the two-temperature stage, when the electron thermal wave propagates from the $\delta_{\text{skin}} \approx 15$ nm skin layer with a supersonic velocity. In the time interval t_{eq}, the absorbed heat penetrates to a depth of $d_T \approx 100$–120 nm. In this case, the average velocity is 30 km/s, which is almost five times higher than the speed of sound. At $t > t_{\text{eq}}$, the thermal wave is transformed to a usual subsonic propagation regime with a low velocity of the thermal wave.

The broadband equation of state of aluminum [5] and data from website [5] supported by Khishchenko et al. were used in the two-temperature hydrodynamic code [3]. The main parameters characterizing the two-temperature state are the electron–ion energy exchange coefficient α and the electron heat conductivity κ_e [3]. The well-known coefficient for aluminum is $\alpha \approx 3.6 \times 10^{18}$ erg s^{-1} cm^{-3} K^{-1} [10]. At a given absorbed fluence F_{abs}, the heating depth d_T and melt thickness d_{m} are determined by the heat conductivity κ_e, because the coefficient α is fixed.

The function $\kappa_e(T_e, T_i, \rho)$ was taken according to the model developed in [11], which ensures the best agreement with the experimental data among the currently existing models. As will be seen below, the two-temperature hydrodynamic calculations with κ_e according to [11] are in good agreement with the experimental data obtained in this work. At a given absorbed fluence F_{abs}, the amplitude and length of the compression wave p_+ shown in Fig. 2 depend on the heating depth d_T: with an increase in d_T, the amplitude of the wave decreases and the length of the wave increases. In turn, the amplitude of p_+ determines the measured velocity u with which the motion of the rear surface begins when the acoustic signal formed at the two-temperature stage arrives at this surface.

It is known [12] that first, the fast heating by femtosecond laser pulses results in a sharp increase in the pressure and the appearance of acoustic waves propagating from the heating layer. Second, the reflection of these waves from the surfaces of the film leads to the displacements of the surfaces. In this work, the displacement $\Delta x(t)$ of the rear surface is considered. We emphasize that the wave profiles in the aluminum film on the glass substrate considered in this work are qualitatively different from those in the free foil investigated in [12]. In the latter case, glass was absent and both surfaces of the aluminum foil are in contact with air at atmospheric pressure.

Figure 2 shows the propagation of the wave p_+ in the film. The time t is measured from the maximum of the intensity of the pump femtosecond laser pulse, which is approximated by the Gaussian $I(t) = I_{\max}\exp(-t^2/\tau_L^2)$ with $\tau_L = 90$ fs and $\tau_{\mathrm{FWHM}} = 150$ fs. Note that the low phonon thermal conductivity of glass was neglected in the two-temperature hydrodynamic calculations. Since the characteristics on the (x, t) plane in linear acoustics are parallel to each other, the traveling wave p_+ has the form $p(x - c_st)$ and its shape is unchanged in time. In the case under consideration, the wave is moderately nonlinear: in contrast to linear acoustics, the characteristics are focusing (approach each other) in the section of an increase in the pressure and defocusing (diverge) in the decrease section. For this reason, the compression wave is broken: the pressure jump is formed and, moreover, the maximum p value decreases with the time and the rear section is stretched along the x axis.

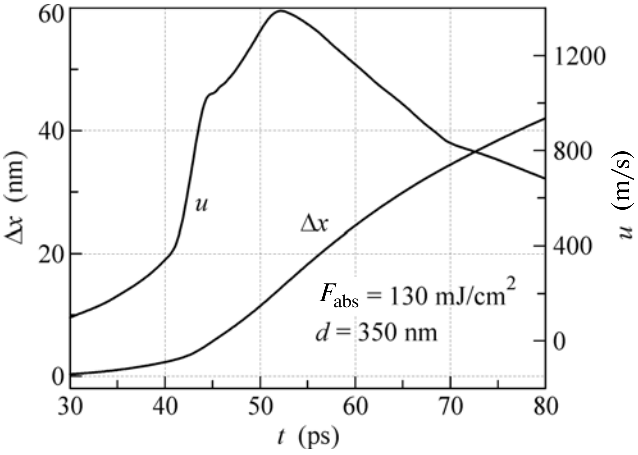

Fig. 3. Displacement $\Delta x(t)$ and velocity $u(t)$ of the rear surface of the film with the thickness $d = 350$ nm. The maximum velocity corresponds to the bend in the $\Delta x(t)$ dependence.

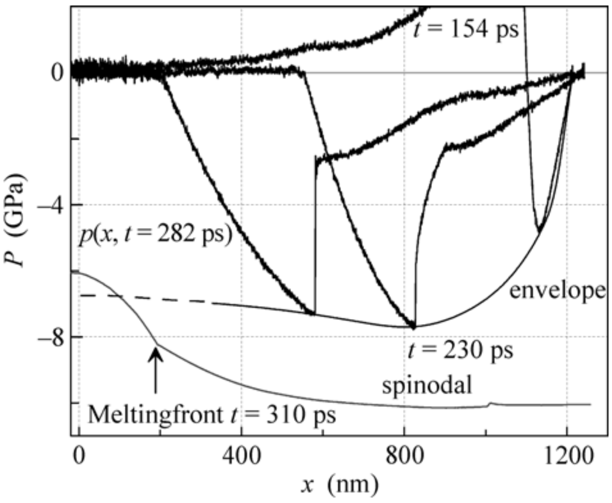

Fig. 4. Spinodal strength $p(x)$ of the inhomogeneously heated aluminum film and the envelope of the wave $p(x, t)$. The idea of the method for the location of the melting front is based, first, on the significant difference between the strengths of the solid and liquid phases and, second, on the fact that the amplitude of the tensile stress varies slowly when the wave propagates. In this method, the amplitude of the wave should be between the nucleation thresholds in the solid and liquid phases, see the main text.

Figure 3 shows the "response" of the rear surface to the reflection of the wave p_+ shown in Fig. 2 from it. In linear acoustics, the functions $p(x - c_st)$ and $u(t) = (d/dt)\Delta x(t)$ are similar at the appropriate scaling of the t and x axes. Figure 3 is presented for a film whose thickness is $d = 350$ nm rather than 1200 nm as in Fig. 2. The compression wave p_+ inducing the displacement $\Delta x(t)$ in Fig. 3 has almost the same profile as the wave in Fig. 2 at the time $t = 20$ ps. Correspondingly, the profile $p(x, t = 20\text{ ps})$ in Fig. 2 and the profile $u(t)$ in Fig. 3 are similar. To illustrate the connections of the femtosecond laser pulse → the compression wave $p(x, t)$ → the displacement $\Delta x(t)$, we took a thinner film, because the structure of the wave $p(x, t)$ is simplified as the wave propagates. Indeed, since the acoustic characteristics approach each other, a thermal precursor in front of the pressure jump is continuously weakened and the pressure increase section between the pressure maximum and pressure jump disappears gradually, cf. the profiles in Fig. 2. Note that as will be shown below, the precursor was not observed in the experiment with the $d = 350$ nm film, because either it was weak or the accuracy of the measurements at small displacements was insufficient.

As is known [4, 6, 12, 13], after reflection from the free surface $x = d$, the compression wave p_+ with $p > 0$ shown in Fig. 2 is transformed into a rarefaction wave p_- with negative pressure $p < 0$ propagating to the left. Figure 4 shows the propagation of the reflected wave from the rear surface towards the melt layer according to the molecular dynamics calculation for the absorbed energy $F_{\mathrm{abs}} = 130$ mJ/cm^2 and film thickness $d = 1200$ nm. The envelope in this figure is plotted through the maxima of the tension in the traveling reflected wave. These maxima increase continuously with the distance from the surface and are saturated at a certain distance from the surface. Such a behavior is due, first, to the boundary condition for the pressure $p(x = x_{\mathrm{rear}}(t), t) = 0$ on the free surface $x = x_{\mathrm{rear}}(t)$ and, second, to saturation reached at the distance of about the finite width of the wave p_+ (see Fig. 2).

The rarefaction wave p_- shown in Fig. 4, as well as the wave p_+ shown in Fig. 2, is moderately nonlinear: its propagation is accompanied by the focusing and defocusing of the characteristics. For this reason, the absolute value of the amplitude of the pressure minimum in Fig. 4 decreases slowly as the wave propagates (after the passage of saturation). In addition, the left side of the wave is stretched, whereas the right side becomes steeper, cf. the wave profiles in Fig. 4. Note that the left side of the reflected wave is an image of the jump in the compression wave p_+ in Fig. 2, whereas the right side is the rarefaction wave on the profile of p_+. As is seen, their character with respect to the focusing/defocusing of the characteristics changes after reflection. The right side of the reflected wave p_- is broken and forms a jump (shock wave), cf. the wave profiles in Fig. 4. The conditions on such a jump correspond to the continuation of the Hugoniot curve behind the binodal to the metastable region. The jump moves more rapidly than the characteristics. Consequently, the depth of the "well" in the pressure in Fig. 4 decreases with time.

In linear acoustics, the amplitude of the wave p_- after the saturation is proportional to the amplitude of the wave p_+. Let us compare the cases with different amplitudes of the wave p_+. When the wave p_+ is sufficiently strong, the negative pressure p_- is higher than the material strength σ_{str}. In this case, spallation occurs on the rear surface. This phenomenon is obviously threshold in the amplitude of p_+ or (equivalently) of p_-. The thickness of the separated (spall) layer d_{sp} at the threshold is determined by the depth at which the saturation discussed above occurs. This depth corresponds to the minimum on the envelope in Fig. 4.

The thickness d_{sp} decreases with an increase in the amplitude of the wave p_+ above the spall threshold. A spall in a homogeneous layer whose strength σ_{str} is independent of the coordinate x is absent below the threshold. An unusual situation arises in the aluminum film heated through glass under consideration. In this case, a hot aluminum layer with the thickness d_T is formed near the interface with glass. It is important that the strength σ_{str} decreases with an increase in the temperature [4, 6]. The strength can be estimated using the spinodal curve $p_{\mathrm{spin}}(T)$. We took it from [5, 14, 15] and the temperature profile $T(x, t)$ from the two-temperature hydrodynamic calculation. Let t correspond to the arrival time of the reflected wave p_- at the melted layer. In Fig. 4, $t = 310$ ps is taken. The temperature at large times of about 100 ps varies slowly; hence, $T(x)$ can be written instead of $T(x, t)$. The calculated function $\sigma(x) = p_{\mathrm{spin}}(T(x))$ is shown in Fig. 4 by the line marked as spinodal.

Let us compare the curves marked as spinodal and envelope in Fig. 4. As is seen, the wave subthreshold with respect to the cold solid phase is superthreshold for a quite hot aluminum melt. This situation is unusual. First, spallation in the solid phase changes to cavitation in the melt and, second, the spall layer is anomalously thick. Indeed, the maximum thickness d_{sp} is determined by the distance from the rear side to the heated layer rather than by the saturation point in Fig. 4. This distance can obviously be large in thick aluminum films. We emphasize that the standard linear formula $\sigma_{\mathrm{lin}} = \rho c_s \Delta u/2$, where Δu is the difference between the velocities at the maximum and minimum of the $u(t)$ dependence exemplified in Fig. 3, is inapplicable to estimate the strength of the melt in the case of deep location. This formula is applicable if spallation occurs in the section of the increase in the amplitude of the tensile stress in the medium. In the case of location, σ_{lin} provides the estimate of the stress sustained by the cold crystal through which the wave p_- has passed, see Fig. 4.

The molecular dynamics calculation of the wave p_- shown in Fig. 4 was performed for the fcc aluminum crystal, which is in equilibrium ($p = 0$) at room temperature before irradiation by femtosecond laser pulses, see [12]. The crystal is oriented in the 111 close packed direction along the hydrodynamic motion axis x. The power E_{ei} transferred from hot electrons to ions at the short two-temperature stage is calculated using the two-temperature hydrodynamic code and is used to simulate heating in the relaxation time t_{eq} in the molecular dynamics code. The important advantage of the molecular dynamics approach is the absence of uncertainties associated with the hydrodynamic description of metastable decay at $p < 0$ in the two-temperature hydrodynamic code.

Figure 5 shows the density distribution at 10 ps after the beginning of cavitation in the melt. In the case under consideration, the amplitude of the tension wave and the strength profile of the melt are such that liquid aluminum is foamed in the entire melt layer. A surprising phenomenon of the propagation of the nucleation front with a high phase velocity to the left is observed owing to an increase in the temperature (decrease in the strength) to the left along the x axis, which compensates a decrease in the amplitude of negative pressure. As mentioned above, the strength profile $\sigma(x)$ is determined by the temperature distribution. The line marked as spinodal in Fig. 4 provides the representation of this profile. Note that the dashed part of the line marked as envelope in Fig. 4 indicates the continuation of the envelope for the case of the absence of nucleation. The amplitude of tension-induced stresses vanishes in the presence of cavitation.

Owing to the abrupt decrease in stresses in the cavitation region, the acoustic signal called the spall pulse is formed and propagates from the cavitation region towards the rear surface. The upward arrow in Fig. 6 marks the time of the arrival of the spall pulse at the rear surface in the solid line, which is obtained by the molecular dynamics simulation. The downward arrow in Fig. 6 marks the time of the beginning of the nucleation shown in Fig. 5. The profile of the acoustic wave corresponding to the spall pulse is complicated owing to the reflection from the melting front. The profile is affected both by the reflection of the leftward moving wave p_- (see Fig. 4) and by the refraction on the melting front of the spall pulse propagating from the interior of the liquid layer to the right. This leads to the appearance of the wide peak in the p_{xx} curve at $x \sim 250$ nm in Fig. 5. Unfortunately, the molecular dynamics data in Fig. 6 are in worse agreement with the experimental data at long times passing from the arrival of the signal at the rear surface. This can be caused by the electron heat conduction disregarded in this molecular dynamics code. The temperature of the liquid phase in the molecular dynamics simulation at long times is correspondingly higher than that in the two-temperature hydrodynamic calculation. Moreover, the heating of glass owing to the partial absorption of a femtosecond laser pulse in glass possibly affects the late evolution. In the arrival time, the experimental signal marked by the vertical linear segment in Fig. 6 is similar to the discontinuity near or at the glass–aluminum interface.

Figure 7 shows the calculations in comparison with the experimental data for two (350- and 1200-nm) aluminum films on glass. The focusing conditions and the energy of the femtosecond laser pulse (64 μJ) are the same for both films. Similar experiments, but without comparison with the theory, were performed in [16] for nickel. In the experimental data, the time t_{exp} is measured from the same time for films with different thicknesses. Unfortunately, the arrival time of the pump femtosecond laser pulse at the glass–aluminum interface with respect to this time is unknown. For this reason, the time t_{exp} in Figs. 6 and 7 is shifted so that the sections to the maximum velocity in the experiment and molecular dynamics simulation coincide with each other for the thinnest film with the thickness $d = 350$ nm.

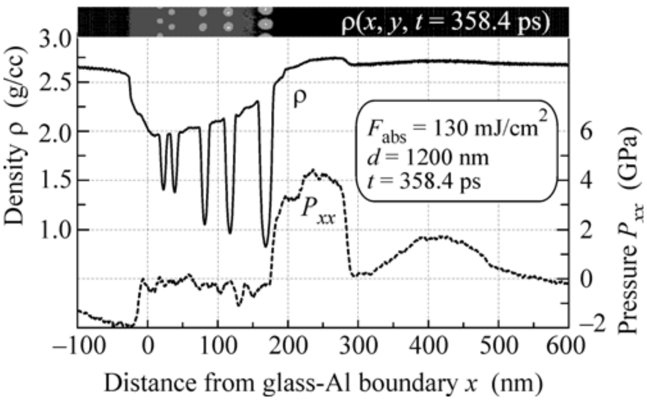

Fig. 5. Density ρ averaged over the (y, z) cross section and pressure in the case of cavitation in the aluminum melt under the action of tensile stresses induced in the melt layer by the wave p_- at $t = 359$ ps. Dips in ρ are attributed to large bubbles.

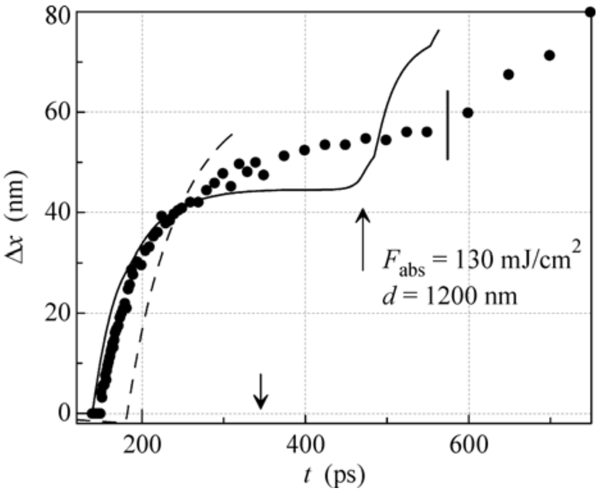

Fig. 6. (Solid line) Molecular dynamics, (dashed line) two-temperature hydrodynamic calculations, and (points) experimental data.

It is seen that the compression wave p_+ in the two-temperature hydrodynamic calculation moves slower (see Fig. 7). The analysis attributes the two-temperature hydrodynamic signal delay increasing with the thickness d to a lower speed of sound in the broadband equation of state used in the two-temperature hydrodynamic calculations. The reason is that the solid medium in the two-temperature hydrodynamic calculation is described in the plastic limit, which is valid only above the dynamic flow limit σ_{el} [4–6]. Elasticity should be taken into account in the flow regions where stresses are lower than this limit. There are phenomenological elastic–plastic models describing the forma-

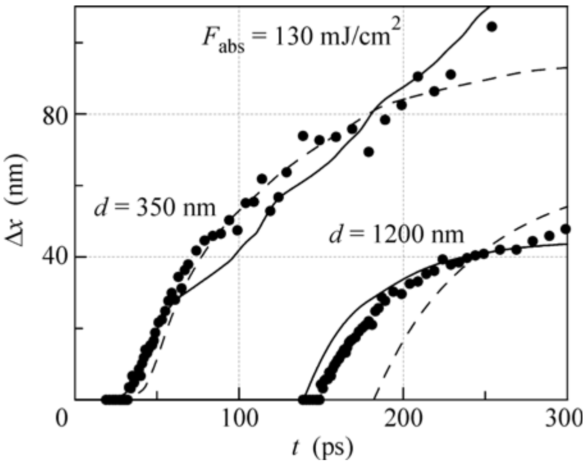

Fig. 7. (Solid line) Molecular dynamics and (dashed line) two-temperature hydrodynamic calculations in comparison with the experimental points. In the molecular dynamics simulation with $d = 350$ nm, nucleation begins at the time $t = 82$ ps and the wave reflected from the melting front and the spall pulse arrive at the rear surface at $t = 92$ and 110 ps, respectively.

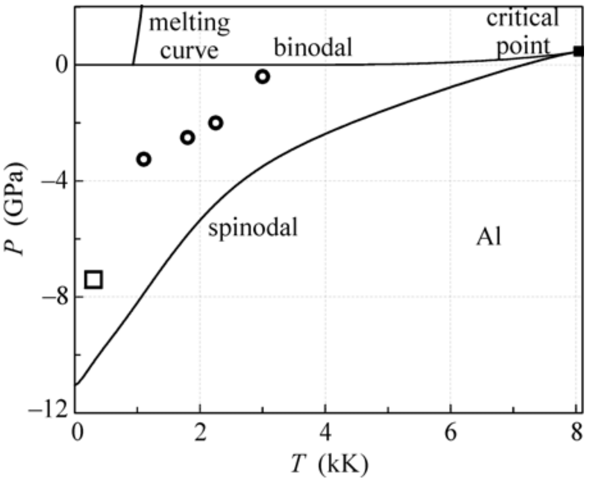

Fig. 8. Calculated strength of the liquid and solid (in the 110 direction) aluminum phases upon tension. The melting curve, bimodal, and spinodal are taken according to [5, 14, 15].

tion of an elastic precursor in front of a plastic shock wave [4]. To apply them in the considered range of ultrahigh strain rates $\dot{V}/V$, large preparatory works with the processing of the molecular dynamics data and/or experimental data should be made in order to extract the phenomenological coefficients entering into the elastic—plastic models. This is a future task. We emphasize that the above molecular dynamics results and experimental data indicate that aluminum remains in the elastic state at sufficiently high pressures that are an order of magnitude higher than σ_{el} values known from the experiments at lower rates $\dot{V}/V$ [4].

It has been shown above that the molecular dynamics calculations with the embedded-atom method potential [12] are in good agreement with the experimental data on the propagation velocity of the wave p_+. Figure 8 shows the molecular dynamics results for the strength of the aluminum melt. The four circles refer to the four nucleation “flashes,” which are seen in Fig. 5. The rates $\dot{V}/V$ corresponding to these points are (in the order of an increase in the temperature) 1.2, 1.9, 2, and 1.5 in units of 10^9 s^{-1}. The square indicates the strength of the aluminum crystal, 7.4 GPa, upon tension in the 110 direction at the rate $\dot{V}/V = 4.3 \times 10^9$ s^{-1} [12]. The calculation reported in [17] yields a strength of 8.4 GPa at a lower temperature of 100 K and the same rate $\dot{V}/V$. In that calculation, it is assumed that the crystal is plastically transformed in the shock wave; this behavior is not observed in our molecular dynamics simulations and experimental data at ultrahigh rates $\dot{V}/V$.

To summarize, (i) the method for the acoustic location of a melt through its thickness has been presented, (ii) it has been shown that the aluminum crystal remains elastic at $p \sim 10$ GPa, and (iii) the strength of the liquid aluminum phase has been determined at ultrahigh rates $\dot{V}/V$.

This work was supported by the Russian Foundation for Basic Research, project no. 09-08-00969-a.

REFERENCES

1. V. V. Temnov, K. Sokolowski-Tinten, P. Zhou, and D. von der Linde, J. Opt. Soc. Am. B **23**, 1954 (2006).
2. M. B. Agranat, N. E. Andreev, S. I. Ashitkov, et al., Pis’ma Zh. Eksp. Teor. Fiz. **85**, 328 (2007) [JETP Lett. **85**, 271 (2007)].
3. N. A. Inogamov, V. V. Zhakhovskii, S. I. Ashitkov, et al., Appl. Surf. Sci. **255**, 9712 (2009); arXiv:0812.2965v1 [physics.optics].
4. G. I. Kanel’, S. Razorenov, and V. E. Fortov, *Shock-Wave Phenomena and the Properties of Condensed Matter* (Springer, Berlin, 2004).
5. A. V. Bushman, G. I. Kanel’, A. L. Ni, and V. E. Fortov, *Intense Dynamic Loading of Condensed Matter* (Taylor Francis, 1993); http://teos.ficp.ac.ru/rusbank/.
6. G. I. Kanel’, V. E. Fortov, S. V. Razorenov, Usp. Fiz. Nauk **177**, 809 (2007) [Phys. Usp. **50**, 771 (2007)].
7. M. Takeda, H. Ina, and S. Kobayashi, J. Opt. Soc. Am. **72**, 156 (1982).
8. D. S. Moore, K. T. Gahagan, J. H. Reho, et al., Appl. Phys. Lett. **78**, 40 (2001).

9. S. I. Anisimov, B. L. Kapeliovich, and T. L. Perel'man, Zh. Eksp. Teor. Fiz. **66**, 776 (1974) [Sov. Phys. JETP **39**, 375 (1974)].
10. Zh. Lin, L. V. Zhigilei, and V. Celli, Phys. Rev. B **77**, 075133 (2008).
11. N. A. Inogamov and Yu. V. Petrov, Zh. Eksp. Teor. Fiz. **137**, 505 (2010).
12. V. V. Zhakhovskii, N. A. Inogamov, Yu. V. Petrov, et al., Appl. Surf. Sci. **255**, 9592 (2009).
13. T. Antoun, L. Seaman, D. R. Curran, et al., *Spall Fracture* (Springer, 2003).
14. M. E. Povarnitsyn, P. R. Levashov, and K. V. Khishchenko, in *Proceedings of the 33th International Conference on Matter State Equations, Physics of Extremal Matter State*, Ed. by V. E. Fortov et al. (El'brus, 2008), p. 161.
15. M. E. Povarnitsyn, K. V. Khishchenko, and P. R. Levashov, Appl. Surf. Sci. **255**, 5120 (2009).
16. D. J. Funk, D. S. Moore, S. D. McGrane, et al., Thin Solid Films **453–454**, 542 (2004).
17. P. A. Zhilyaev, A. Yu. Kuksin, V. V. Stegailov, and A. V. Yanilkin, Fiz. Tverd. Tela (2010, in press).

Translated by R. Tyapaev